Lab on a Chip

PAPER

View Article Online
View Journal | View Issue

Cite this: *Lab Chip*, 2025, **25**, 6517

An ischemic stroke-on-a-chip model integrated with machine learning for screening of drug candidates

Jiayue Liu,†[ab] Peng Wang,†[ab] Peihan Lian[ab] and Jianhua Qin *[abc]

Received 26th May 2025,
Accepted 21st October 2025

DOI: 10.1039/d5lc00517e

rsc.li/loc

Ischemic stroke is a leading cause of death and long-term disability worldwide, characterized by the sudden loss of cerebral blood flow, resulting in energy failure, oxidative stress, inflammation, and blood–brain barrier (BBB) disruption. Despite their clinical significance, current preclinical models inadequately recapitulate the multifaceted pathophysiology of cerebral ischemia, hindering systematic therapeutic exploration. Here, we engineered a human iPSC-derived BBB-on-a-chip (iBBB-on-a-chip) platform that can simulate ischemic pathology through controlled oxygen–glucose deprivation. The model exhibited characteristic features of ischemia-induced BBB impairment, including disruption of endothelial tight junctions, pericyte fragmentation, and increased permeability. By integrating transcriptomic profiling with a weighted gene co-expression network analysis algorithm, we identified stroke-related pathways and applied machine learning (random forest and LASSO) to screen hub genes for biomarker discovery. Using the Connectivity Map database and molecular docking calculations, we identified coumarin as a potential therapeutic agent and experimentally confirmed its protective role in the iBBB-on-a-chip. This strategy establishes a novel paradigm combining organ-on-a-chip technology with machine learning-driven data analysis, creating an innovative platform for the study of cerebrovascular disease and drug screening.

1 Introduction

Ischemic stroke is one of the leading causes of high mortality and long-term disability worldwide, posing a significant burden.[1,2] In the early stage of ischemic stroke, the local brain tissue is insufficient in oxygen and nutrient supply due to blood flow restriction, which induces a series of cascade reactions, including oxidative stress, inflammatory activation, and blood–brain barrier (BBB) destruction. As the critical component of the neurovascular unit, the BBB is a highly specialized structure that regulates the exchange of nutrients, metabolites, and ions while preventing harmful substances from entering the central nervous system (CNS).[3–8] The BBB is mainly composed of human brain microvascular endothelial cells (HBMECs), the extracellular matrix (ECM), pericytes, and astrocytes.[8,9] Normally, these cells collectively maintain the structural stability and functional integrity of the BBB. Its dysfunction not only fuels the pathological progression of stroke but also affects the delivery and effectiveness of potential therapeutic drugs (Fig. 1a).[10]

Despite the pivotal role of the BBB in stroke pathology, current models for studying ischemic BBB dysfunction remain inadequate. Animal models, although invaluable for understanding the complex interaction of neurovascular units, face translational limitations due to interspecies differences in gene expression patterns, anatomical structures, and physiological processes.[11,12] Additionally, their time- and cost-intensive nature limits their utility for therapeutic screening. On the other hand, traditional *in vitro* BBB models fail to replicate critical microenvironmental factors like shear stress, oxygen gradients, and dynamic cell–cell interactions, which are essential for mimicking ischemic stroke conditions.[13–15]

Recent advances in organ-on-a-chip technology offer a promising solution to overcome the limitations of traditional models by precisely recreating physiological microenvironments.[16–20] BBB-on-a-chip platforms can replicate the human-specific BBB architecture and its dynamic responses to ischemic insults, providing a powerful platform for investigating neurovascular pathophysiology and evaluating potential therapies.[21–24] However, to fully leverage these models, advanced data analysis approaches are required to interpret complex

[a] *School of Biomedical Engineering, Division of Life Sciences and Medicine, University of Science and Technology of China, Hefei, Anhui, 230026, P.R. China. E-mail: jhqin@dicp.ac.cn*
[b] *Suzhou Institute for Advanced Research, University of Science and Technology of China, Suzhou, Jiangsu, 215123, P.R. China*
[c] *Division of Biotechnology, Dalian Institute of Chemical Physics, Chinese Academy of Sciences, Dalian, Liaoning, P.R. China*
† These authors contributed equally to this paper.

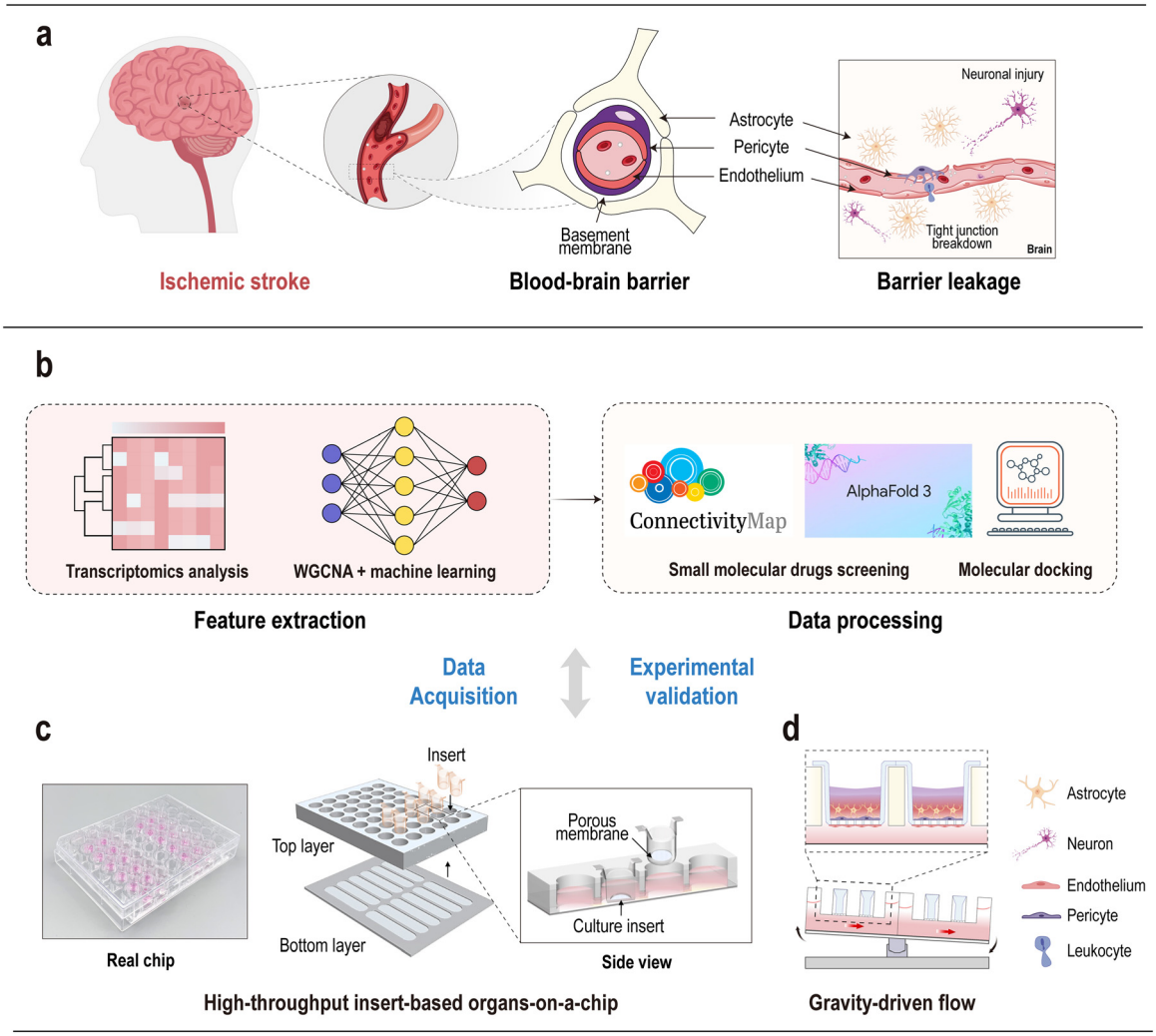

Fig. 1 Overview of the ischemic stroke-on-chip and machine learning-assisted analysis pipeline. a. Schematic diagram of *in vivo* ischemic stroke pathology, highlighting BBB disruption following ischemic insult. b. Working pipeline for the ischemic stroke-on-chip. This panel details the complete workflow of the ischemic stroke-on-chip system, from cell culture and transcriptomics analysis to WGCNA, machine learning-based biomarker prediction, and therapeutic drug screening. c. Configuration of the chip design and assembly. This panel illustrates the organ-on-a-chip system design, featuring multiple culture units with a culture chamber, medium reservoir, and bottom flow channel. The porous membrane separates the culture chamber from the flow channels, enabling cell culture and fluid movement. The insert provides a flexible 3D culture environment, enabling more realistic simulation of the BBB under dynamic conditions. d. Seeding and co-culture of induced iBBB cells on chip. iPSCs are differentiated into iBMECs (induced brain microvascular endothelial cells), iPericytes (induced pericytes), and astrocytes (induced astrocytes) for co-culture in the chip model, recapitulating the BBB components. The chip setup includes both static conditions and gravity-driven flow conditions, enabling the dynamic culture of iBBB cells in the system. Blood–brain barrier, BBB.

biological responses. With the development of high-throughput sequencing technology, how to identify hub genes closely related to disease progression from large-scale and multi-dimensional omics data has become an important challenge in neurovascular research.[25–27] Machine learning algorithms have shown strong performance in extracting disease-relevant gene signatures, which can be reverse-matched with drug databases and refined using molecular docking, thereby enhancing the accuracy and efficiency of data-driven drug screening.

In this study, we designed a novel paradigm converging organ-on-a-chip technology with artificial intelligence to deconvolute ischemic stroke pathophysiology. We engineered a human iPSC-derived BBB-on-a-chip (iBBB-on-a-chip) that recapitulates cerebral hypoperfusion dynamics through biomimetic shear stress and metabolic challenge protocols. This iBBB-on-a-chip was integrated with transcriptomic profiling and co-expression network analysis to identify core molecular pathways, followed by machine learning-based hub gene prioritization and computational drug screening. Through this integrated pipeline—encompassing model construction, biomarker discovery, therapeutic prediction, and experimental validation—we aimed to bridge the gap between physiological modeling and data-driven therapeutic discovery (Fig. 1b).

2 Methods

2.1 Cell culture

To induce the differentiation of iPSCs into BBB-relevant HBMECs, we employed a hypoxia-enhanced protocol adapted from a previously reported method. iBMECs were cultured under reduced O_2 (1–8%) to mimic the physiological oxygen levels of the brain microenvironment.

iPSCs (#CN-IPS) were a kind gift provided by Prof. Jianwen Deng (Peking University First Hospital) and were propagated on a six-well plate that was coated with Matrigel (Gibco, CAS No. 354230) by using an mTeSR1 medium (Stem Cell Technology) and maintained according to the protocol of the hypoxia-enhanced procedure.[28] iBMECs were cultured on T75 precoated flasks with Matrigel diluted at 1 : 100 in DMEM/F12 (D/F12), which were maintained in an endothelial cell medium (ECM; number 1001; ScienCell) supplemented with 10% FBS, 1% ECGS and 1% P/S. iAstrocytes were cultured on T75 precoated flasks with Matrigel diluted at 1 : 100 in DMEM/F12 (D/F12), which were maintained in an astrocyte medium (AM) (ScienCell, 1801) supplemented with 2% FBS, 1% AGS and 1% P/S. hPSC-PCs (iPericytes) were grown on T75 precoated flasks with 2%, which were a kind gift from Prof. Andy Peng Xiang's laboratory (Sun Yat-Sen University) and were cultured in PM medium (number 1201; ScienCell). hPSC-PCs were transfected with a lentivirus-GFP vector for 48 h, and GFP + hPSC-PCs were selected with 10 μg mL^{-1} puromycin dihydrochloride (Beyotime; Cat #: ST551). Except for the specially differentiated iBMECs, all other cells were cultured at 37 °C in a humidified atmosphere of 20% CO_2. T75 flasks coated with collagen were prepared by incubation at 4 °C overnight.

2.2 Chip fabrication

We used SolidWorks software to design the structure of the chip. It was sent to Dalian Xinglin Factory for machining. Ultra-thin double-sided adhesive (Adhesive Research) was precisely applied to the defined regions using a fully automated dispensing system, which was subsequently used to assemble and seal the chip. The chip dimensions, materials, fabrication protocols, flow rates, and shear stress parameters were shown in our previous study.[29] Before cell culture, the chips were sterilized using ethylene oxide gas.

2.3 Cell culture on organs on chip

Human induced pluripotent stem cells (hiPSCs, CN-IPSC line, a gift from Prof. Jianwen Deng, Peking University First Hospital, passage number 25–30) were cultured on Matrigel-coated (Gibco, Cat# 354230) 6-well plates using an mTeSR1 medium (Stem Cell Technologies) at 37 °C with 5% CO_2. Cells were passaged at 1.8×10^5 cells per well and maintained until confluence (~2.5×10^5 cells per well).

To initiate endothelial differentiation, confluent iPSCs were cultured under hypoxia (5% O_2) for 3 days in mTeSR1, and then switched to unconditioned endothelial induction medium (Table S1) for 6 days. After 6 days of differentiation, cells were transitioned to endothelial expansion medium (Table S2) for 2 days of further maturation. Then wait for the iBMECs to be seeded on the iBBB-on-a-chip and use an endothelial maintenance medium (Table S3) for culture maintenance.

iAstrocytes, kindly provided by Prof. Wenyuan Wang (Shanghai Institute of Organic Chemistry, Chinese Academy of Sciences), were cultured under standard conditions using an astrocyte medium (AM; ScienCell, Cat. No. 1801) supplemented with 2% fetal bovine serum, 1% astrocyte growth supplement, and 1% penicillin–streptomycin.

iPericytes (hiPSC-derived pericytes) were provided by the team of Professor Xiang Peng of Sun Yat-Sen University and cultured in PM medium (ScienCell, Cat. No. 1201) in 1% Matrigel pre-coated T75 bottles. iPericytes were screened using 10 μg mL^{-1} puromycin (Beyotime, Cat. No. ST551) to obtain GFP + cells after 48 h of GFP lentiviral infection.

To construct the iBBB-on-a-chip, cell culture inserts were pre-coated to enhance cell adhesion and mimic the extracellular environment. The upper surface of the culture insert was coated with 1% poly-D-lysine (PDL), while the lower surface was coated with 1% Matrigel (Gibco, CAS No. 354230), to provide a supportive matrix for cell attachment and growth. Coating was performed at 37 °C overnight before seeding the cells. iBMECs (5×10^4 cells per well) were initially added onto the bottom side of the insert and the cells were allowed to attach to the membrane surface. Two hours later, the inserts were transferred to a high-throughput fluidic plate, and 1 mL ECM medium was added into the lower well. Then, 200 μL of brain cell mixture suspension (iAstrocyte cells: 200 cells per μL; hPSC-PCs: 20 cells per μL) was added into the upper well of the insert. The brain medium was a mix of AM and PM media (AM : PM = 1 : 1), and the medium was changed every two days. After one day of static culture, the chip was cultured under fluidic conditions (tilting angle = 5°; rocking frequency = 2 Hz) at 37 °C for 4 days to form a functional BBB interface.

We estimated the shear stress (τ) using the formula:

$$\tau = 2\pi f \cdot \mu \cdot \frac{A}{h^2}$$

where τ is the shear force (Pa), f: oscillation frequency (Hz, 2 Hz in this study), μ: medium viscosity, approximation of the viscosity of the water taken (0.001 Pa s), A: liquid oscillation amplitude (m, approximately converted from the inclination angle to the radius of the liquid surface, 5° corresponds to about 1–2 mm), and h: liquid height (m, about 3 mm in this experiment).

2.4 Glucose–oxygen deprivation exposure

To induce ischemic conditions, the chips were placed into a CO_2 laboratory incubator (MCO-170AICUVL-PA, PHCBI Corp.) with 1% O_2 and 5% CO_2 for 24 h.[30,31] Before the chips were placed in the incubator, the culture medium was replaced with serum- and glucose-free DMEM (Gibco, CAS No.

11966025) to simulate ischemia. For chips under normoxic conditions, the culture medium was replaced with basic DMEM (Gibco, CAS No. C11885500BT).

2.5 Immunofluorescence imaging

Cells on the insert chambers were washed twice with phosphate-buffered saline (PBS) and fixed with 4% paraformaldehyde (PFA) at 4 °C overnight. Following fixation, cells were permeabilized and blocked using 0.2% Triton X-100 in PBS (PBST) supplemented with 10% normal goat serum for 30 minutes at room temperature. Antibodies were diluted with PBST buffer and added into the apical and basal chambers, respectively. Cells were stained with the primary antibodies at 4 °C overnight and the corresponding secondary antibodies at room temperature for 2 h. Finally, the cells were counterstained with DAPI, and the insert chambers were mounted onto glass coverslips. Images were acquired using a Leica STELLARIS 5 confocal fluorescence microscope.

2.6 Transmission electron microscopy

After 24 h of oxygen–glucose deprivation (OGD) exposure, culture inserts containing cells were carefully retrieved from the chip and fixed in PBS buffer containing 2.5% glutaraldehyde (Electron Microscopy Sciences) at 4 °C overnight. Samples were subsequently washed three times with PBS and post-fixed in 1% OsO_4 buffer for 2 h at room temperature. Following fixation, the samples were dehydrated with graded ethanol solutions and then embedded in Epon812 resin (SPI). Ultrathin sections (70 nm) were stained with 2% uranyl acetate for 30 minutes, followed by lead citrate for 10 minutes. Images of the chip were acquired using a JEM-1400PLUS electron microscope.

2.7 Permeability assay

The permeability of the iBBB-on-a-chip was evaluated by measuring the diffusion of fluorescently labeled dextrans—10 kDa cascade blue-dextran and 70 kDa Texas red-dextran—from the vascular (lower) to the brain (upper) channel. Briefly, an ECM medium containing 100 μg mL^{-1} dextran was added into the lower blood channel. After 2 h incubation at 37 °C, the media in the upper brain channel were collected for analysis. The concentrations of 10 kDa cascade blue-dextran were determined by fluorescence intensity using a microplate reader system at 400 nm (excitation) and 440 nm (emission). Similarly, the concentrations of 70 kDa Texas red-dextran were determined by fluorescence intensity using a microplate reader system (excitation: 595 nm; emission: 630 nm). The apparent permeability coefficient ($\boldsymbol{P}_{app}$) was calculated according to the equation below:[3,32]

$$\boldsymbol{P}_{app} = \frac{\boldsymbol{V}_u \boldsymbol{C}_u}{\boldsymbol{A}\boldsymbol{C}_l \boldsymbol{t}}$$

$\boldsymbol{V}_u$ (μL): volume of the receiving compartment (upper brain channel); $\boldsymbol{C}_u$ (μg mL^{-1}): concentration of FITC-dextran in the receiving compartment; $\boldsymbol{A}$ (cm^2): area of the transwell membrane (0.336 cm^2); $\boldsymbol{C}_l$ (μg mL^{-1}): initial concentration of FITC–dextran in the donor compartment (lower vascular channel); $\boldsymbol{t}$ (s): time of diffusion (7200 s).

2.8 RNA extraction and qRT-PCR

Total RNA was isolated separately from iBMECs and brain cells using a TRIzol reagent (Invitrogen) as described previously.[33] cDNA synthesis was performed using a PrimeScript RT Master Mix kit (TaKaRa; Cat #: RR036A) and quantitative PCR was performed using a TB Green Premix Ex Taq II kit (TaKaRa; Cat #: RR820A). Primers corresponding to target genes are shown in Table S4.

Initially, GAPDH was used as the reference gene for normalization. Due to the potential variability of GAPDH under hypoxia, we conducted a validation study to identify the most stable internal control for OGD conditions. RPLP1, TBP, and RPLP13A were selected as the candidate housekeeping genes to be evaluated in both normoxic and OGD-treated cells. Expression stability was assessed by comparing C_t variations and reference gene stability rankings. RPLP1 exhibited the most consistent C_t values across experimental conditions and was therefore selected as the reference gene for normalizing qPCR analyses.

2.9 RNA extraction, library preparation and sequencing

Twenty-four hours after OGD treatment, iBMECs and brain cells were collected from the lower vascular channel and upper brain channel, respectively. Total RNAs were extracted using TRIzol (Invitrogen) following the methods of Chomczynski *et al.* (Chomczynski and Sacchi, 1987). RNA samples were treated with DNaseI for DNA digestion and then determined by examining A260/A280 using a Nanodrop OneC spectrophotometer (Thermo Fisher Scientific Inc). RNA integrity was confirmed by 1.5% agarose gel electrophoresis. Finally, qualified RNAs were quantified using Qubit 3.0 with a Qubit RNA Broad Range Assay kit (Life Technologies).

Samples with 2 μg total RNA were used for stranded RNA sequencing library preparation using a KC-Digital Stranded mRNA Library Prep Kit for Illumina (Catalog No. DR08502, Wuhan Seqhealth Co., Ltd. China), following the manufacturer's instructions. The kit eliminates duplication bias in PCR and sequencing steps by using a unique molecular identifier (UMI) of 8 random bases to label the pre-amplified cDNA molecules. The library products corresponding to 200–500 bps were enriched, quantified, and finally sequenced on a Hiseq X 10 sequencer (Illumina).

2.10 Drug testing

Drug intervention experiments were conducted in two sequential phases to evaluate the therapeutic efficacy of candidate compounds under ischemia–reperfusion (I/R) conditions using the iBBB-on-a-chip model. In phase I, coumarin and everolimus were administered after OGD exposure to assess the temporal drug response at three

reperfusion time points: 3 h, 9 h, and 24 h. Based on these results, 24 h post-OGD was selected as the representative therapeutic window for downstream evaluation. In phase II, four compounds, coumarin, NXY-059, minocycline, and butylphthalide, were tested under standardized treatment conditions. All drugs were applied immediately after the OGD phase and maintained during the 24 h reperfusion period. Drug treatments were delivered through the vascular channel of the chip to mimic systemic administration. Detailed concentrations for each compound are provided in Table S5.

2.11 LDH activity assay

To evaluate cellular injury, lactate dehydrogenase (LDH) activity in the culture supernatants was measured as an indicator of cellular injury. For baseline experiments, an LDH Activity Assay Kit (E-BC-K046-M, Elabscience, China) was used according to the manufacturer's instructions. For drug validation and extended time-point studies, an LDH Activity Assay Kit (BC0685, Solarbio, China) was applied to ensure batch consistency across experimental repeats.

Culture supernatants were collected separately from the iBMEC and brain cell (iPericytes and iAstrocytes) compartments of the chip. LDH activity was measured at defined time points following OGD, OGD–reperfusion (OGD + I/R), and/or drug treatments. All results were normalized and expressed in serum-equivalent LDH activity units, following kit-specific calculations. Each condition included at least three biological replicates.

2.12 RNA-sequence analysis

Bulk RNA-seq was conducted by Seqhealth Technology Co., Ltd. (Wuhan, China) using a DNBSEQ-T7. Firstly, to discard the low-quality reads and adaptor sequences, raw sequencing data were filtered using Trimmomatic (version 0.36). Subsequently, in-house scripts were further processed using custom scripts to mitigate duplication bias introduced during library preparation and sequencing. In summary, clean reads were initially clustered based on unique molecular identifiers (UMIs), grouping reads with identical UMI sequences. Within each cluster, reads underwent pairwise alignment, and those with over 95% sequence identity were consolidated into new sub-clusters. Multiple sequence alignment was then applied to each sub-cluster to derive a consensus sequence, effectively minimizing errors and biases introduced by PCR amplification and sequencing.

Standard RNA-seq analysis was applied to treat the deduplicated consensus sequences. They were mapped to the reference genome of *Homo sapiens* from the Ensembl database using STAR aligner v.2.5.3a (default parameters). The following data processing was performed using the R project (R version 4.4.0). Unique gene hit counts were obtained using the featureCounts function from the Subread package (version 1.5.2) and then RPKM was calculated. Differential expression analysis was then performed using the edgeR package (version 3.12.1). Significant differential expression analysis (DEGs) was defined with a P-value < 0.05 and the absolute value of $\log_2$(fold change) > 1 as the threshold. GO and KEGG enrichment analyses of DEGs were implemented using KOBAS software (v.2.1.1) with a P-value cut-off of 0.05 to determine statistical enrichment.

2.13 WGCNA (weighted gene co-expression network analysis)

To identify gene modules associated with ischemic injury, WGCNA was applied to transcriptome data from iBMECs and brain cells under OGD conditions. The soft-thresholding power (β) was chosen based on the scale-free topology requirement. Co-expression modules were found utilizing the topological overlap matrix (TOM) and hierarchical clustering. Module–trait correlations were used to identify ischemia-associated modules. Genes from major modules were combined with DEGs to identify hub genes for further investigation.

2.14 Identification of hub genes by machine learning

The random forest approach was used to prioritize the relevance of genes in the target module based on mean decrease accuracy and mean decrease Gini scores. To find statistically significant predictors, these results were refined using least absolute shrinkage and selection operator (LASSO) regression. All of the two analyses were used by the R package "randomForest" and "glmnet". The intersection of hub genes resulting from these two methods was represented by a Venn diagram constructed by the R package "ggvenn", which highlighted five consensus hub genes.

2.15 Small-molecule compound screening and molecular docking

We input 126 hub genes filtered by WGCNA and DEGs into the Connectivity Map (CMap) platform (https://clue.io/) to identify candidate small-molecule compounds with the potential to reverse disease-related gene expression profiles. Compounds with negative connectivity scores were considered as promising candidates for reversing the pathological state. The chemical structures of the identified small molecules were retrieved from PubChem (https://pubchem.ncbi.nlm.nih.gov/). Hub protein three-dimensional (3D) structures were sourced from the AlphaFold Protein Structure Database (https://alphafold.ebi.ac.uk/) and the RCSB Protein Data Bank (https://www.rcsb.org/). Using PyMOL, protein structures underwent preprocessing, such as ligand removal and dehydration, before being transformed into the appropriate docking formats. For cross-validation, molecular docking was carried out utilizing two complementary software platforms. Docking scores were computed to evaluate binding affinities in Sybyl-X, where Surflex-Dock was used to model drug–protein binding based on cavity recognition. For further docking validation,

AutoDock Vina was used to dock the ligands and proteins, and docking simulations were run with default settings.

2.16 Statistical analyses

The data were collected and organized using Microsoft Excel. The data were statistically analyzed using GraphPad Prism 10 software. Each experiment was carried out at least three times. Throughout the experiment and the analysis of the findings, the researchers were blind to the group assignment. The differences between the two groups were examined using Student's *t*-test. Multiple groups were compared using the Bonferroni *post hoc* test and one-way analysis of variance (ANOVA). The data are shown as the mean ± standard error of the mean (SEM). Asterisks indicate importance: *: $P < 0.05$, **: $P < 0.01$, ***: $P < 0.001$.

3 Results

3.1 Establishment of a biomimetic BBB-on-a-chip using iPSCs

We firstly engineered a high-throughput insert-based microfluidic chip comprising two channels: an upper channel

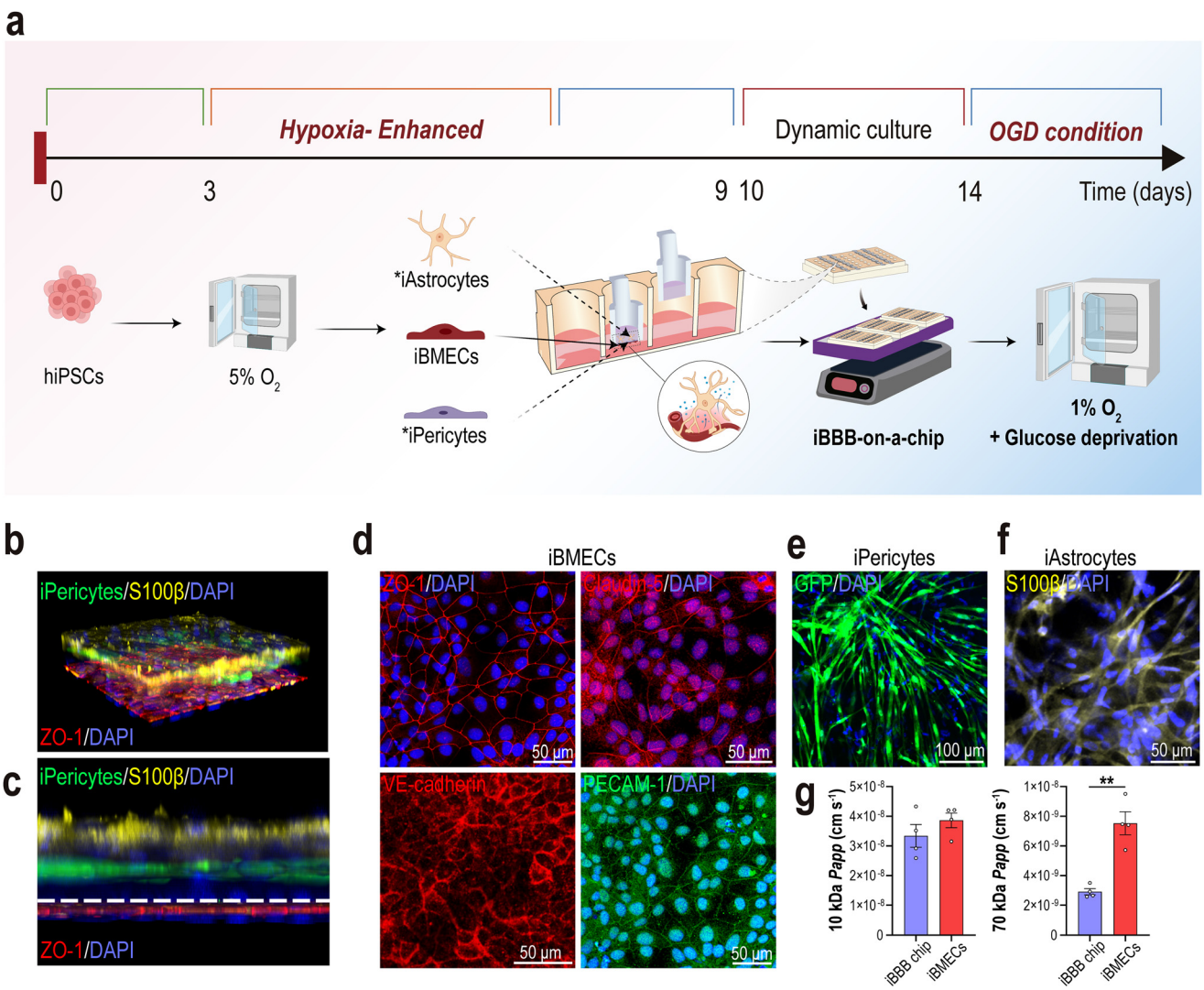

Fig. 2 Establishment of an iPSC-derived BBB-on-a-chip. a. Experimental timeline and protocol illustrate the experimental timeline for culturing iPSCs and iBMECs, and establishing the iBBB-on-a-chip under OGD conditions. b and c. 3D and side-view immunofluorescence images of the iBBB model showing co-localization of pericytes (S100β, green), astrocytes (S100β, yellow), and endothelial tight junction protein ZO-1 (red) at the BBB interface under flow conditions. The white dotted line represents the location of the porous membrane separating the brain (top) and vascular (bottom) compartments in the chip. d. Immunofluorescence images of iBMECs showing the expression of ZO-1, claudin-5, VE-cadherin, and PECAM-1, confirming barrier integrity and the endothelial phenotype. Scale bars: 50 μm. e. Immunofluorescence staining of iPericytes showing GFP expression, demonstrating pericyte differentiation and morphology. Scale bar: 100 μm. f. Immunofluorescence image of iAstrocytes showing S100β expression. Scale bar: 50 μm. g. Dextran permeability assay (10 kDa and 70 kDa) comparing the iBBB-on-a-chip and iBMECs. Data represent the mean ± SEM (n = 4), analyzed with unpaired Student's *t*-test. *: $P < 0.05$, **: $P < 0.01$, ***: $P < 0.001$. Representative images were obtained from three independent experiments. Cells marked with an asterisk and those linked by dashed arrows were gifted from external laboratories. Oxygen–glucose deprivation, OGD.

that supports 3D cell culture embedded in a hydrogel matrix to form endothelial-like structures, and a lower channel that facilitates fluid flow and shear stress to better mimic the *in vivo* environment (Fig. 1c). To replicate the complex structure and function of the human BBB *in vitro*, we developed a human induced pluripotent stem cell (iPSC) derived BBB-on-a-chip (iBBB-on-a-chip) platform, which integrates human brain microvascular endothelial cells (iBMECs), pericytes (iPericytes), and astrocytes (iAstrocytes) within a microfluidic device (Fig. 1d).

To improve cellular organization and functional maturation, we further incorporated a hypoxia-enhanced differentiation strategy into our experimental system (Tables S1–S3). As shown in Fig. 2a, the differentiation process was conducted under fluidic conditions with controlled shaking (swing angle: 5°, swing frequency: 2 Hz) using a customized shaker, which improved the formation of a functional BBB architecture.

After 4 days of culture within the fluidic conditions, three-dimensional and side-view immunofluorescence images confirmed the successful formation of a functional BBB with the co-localization of ZO-1 (an endothelial tight junction marker), S100β (an astrocyte marker), and GFP-labeled pericytes under flow conditions (Fig. 2b and c). Well-developed adherens junctions (VE-cadherin) and tight junctions (ZO-1, Claudin-5) were formed in the brain microvascular endothelial cells (iBMECs), as shown by immunofluorescence staining. Additionally, PECAM1, a key endothelial cell marker, was also positively stained, further confirming the endothelial-like characteristics of the iBMECs (Fig. 2d). iPericytes were identified by the labeled GFP to show their differentiation and morphology (Fig. 2e), while induced astrocytes (iAstrocytes), cultured within Matrigel, expressed S100β (yellow), displaying a star-shaped morphology (Fig. 2f). The co-culture of iBMECs, iPericytes, and iAstrocytes was designed to simulate brain parenchyma and recapitulate the cellular interactions that occur in the brain's microvascular environment. Furthermore, dextran permeability assays (10 kDa and 70 kDa) demonstrated that the multicellular iBBB-on-a-chip model exhibited significantly enhanced barrier integrity compared to iBMEC monocultures, highlighting the contribution of supporting brain cells (iPericytes and iAstrocytes) to BBB function (Fig. 2g). These findings emphasize the importance of cellular integration in recapitulating physiologically relevant barrier properties.

3.2 Modeling the pathological features of ischemic stroke on the iBBB-on-a-chip

To simulate the pathological microenvironment associated with cerebral hypoxia and ischemia, and to assess BBB responses under injury conditions, we first established a functional BBB phenotype over four days in the iBBB-on-a-chip system. We then induced ischemic injury by exposing the model to 1% O_2, serum depletion, and glucose deprivation for 24 h under static conditions. These conditions were designed to simulate the OGD environment characteristic of neurovascular injury under ischemic stress.

Immunofluorescence analysis revealed significant alterations in the BBB architecture under ischemic conditions. Specifically, we observed a loss of endothelial tight junction integrity, as indicated by a marked reduction in ZO-1 expression in iBMECs (Fig. 3a). This disruption was accompanied by pericyte detachment, a phenomenon often associated with vascular instability (Fig. 3b). Additionally, astrocytes (iAstrocytes), identified by S100β staining, exhibited morphological changes, further reflecting the disrupted cellular interactions within the BBB under ischemic conditions. Transendothelial electrical resistance (TEER) measurements, a simple, label-free and non-invasive method to quantify the barrier integrity, further confirmed barrier disruption, with ischemia resulting in a dramatic reduction in TEER values (Fig. 3c). Additionally, the ischemic microenvironment induced a significant increase in cell death across all cell types, as evidenced by live/dead assays. Quantitative analysis revealed that iBMECs were the most susceptible to ischemic injury, followed by iPericytes and iAstrocytes (Fig. 3d and e). This differential vulnerability underlines the unique responses of various cell types within the BBB to ischemic stress. Ischemia also triggered an upregulation of pro-inflammatory markers in endothelial cells. Immunofluorescence staining for VCAM-1 and ICAM-1 demonstrated significantly increased expression levels under ischemic conditions, indicating an activated inflammatory state (Fig. 3f and g). Such changes are consistent with the role of these adhesion molecules in promoting leukocyte adhesion and extravasation during ischemic injury.[34–36]

Transmission electron microscopy (TEM) provided further insights into the ischemic-induced damage at the ultrastructural level. Tight junctions, essential for maintaining BBB integrity, appeared disrupted, with disorganized junctional complexes and cytoskeletal rearrangements in iBMECs (Fig. 3h and i). Additionally, iAstrocytes exhibited mitochondrial swelling and increased vesicular structures, indicative of cellular stress. These ultrastructural alterations closely mimic *in vivo* observations in ischemic stroke-on-chip models. This result also reflected the feasibility of using the iBBB-on-a-chip to probe the BBB dysfunction following neurovascular injury.

3.3 Transcriptomic profiling unveils coordinated cellular efforts to mitigate ischemic stress

To gain mechanistic insights into how different cell types respond to ischemic injury, we conducted transcriptome profiling of iBMECs and brain cells (iPericytes and iAstrocytes) in the iBBB-on-a-chip to investigate the molecular fingerprints underlying BBB dysfunction. Hierarchical clustering illustrated different gene expression patterns between normoxic and ischemic conditions ($P < 0.05$, fold change > 1) (Fig. 4a). Venn diagram analysis and FC-FC plots

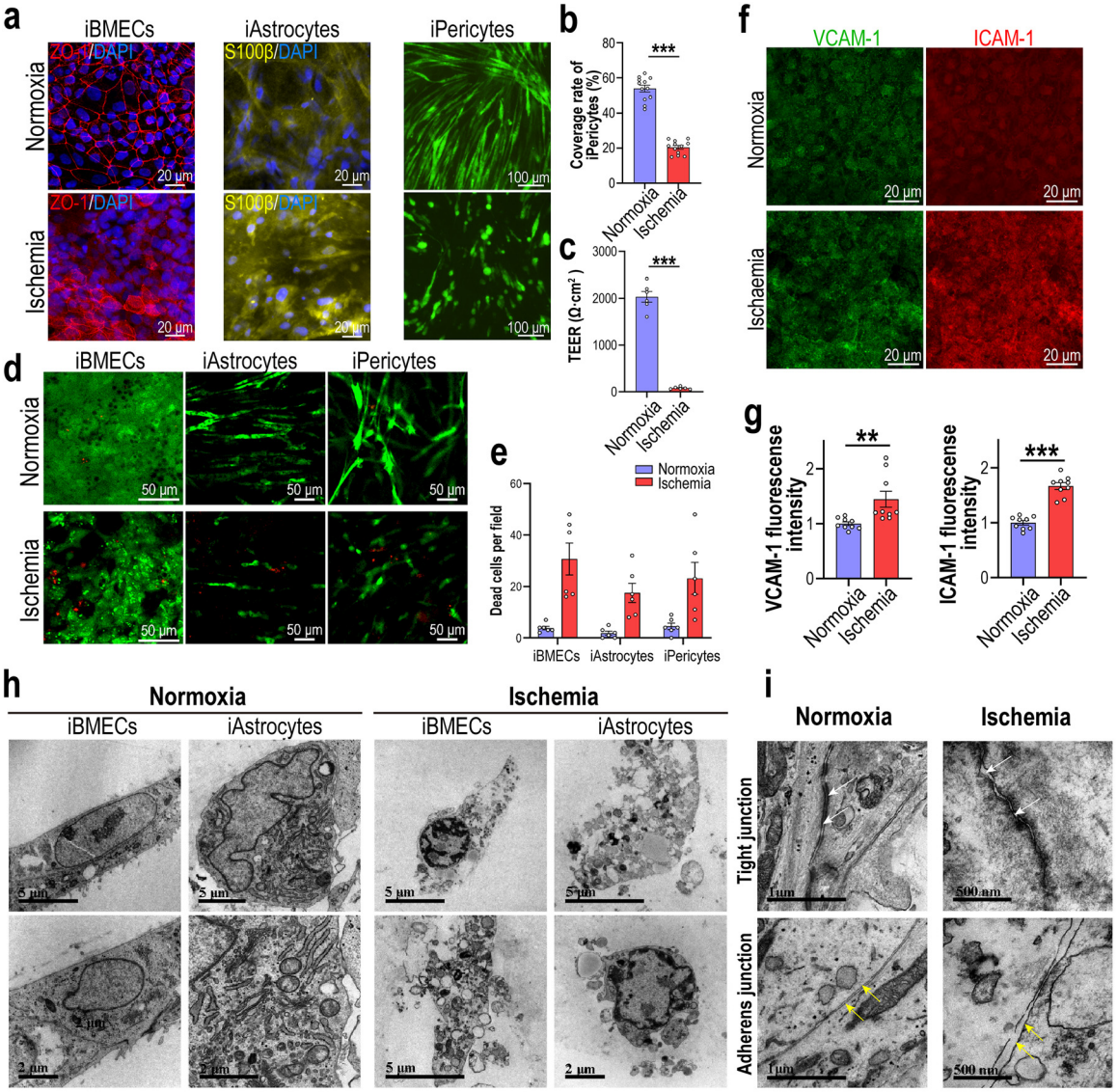

Fig. 3 Pathological characterization of ischemic stroke using the iBBB-on-a-chip. a. Representative immunofluorescence images showing localization of ZO-1 in iBMECs and S100β in iAstrocytes, and morphology of iPericytes under normoxic and ischemic conditions. Scale bars: 20 μm for ZO-1 and S100β, and 100 μm for iPericytes. b. Quantification of pericyte coverage area under normoxia and ischemia. c. TEER of the iBBB-on-a-chip under normoxia and ischemia. d. Live/dead assay images of iBMECs, iPericytes, and iAstrocytes highlighting increased cell death under ischemic conditions. Scale bars: 50 μm. e. Quantification of dead cells per field for iBMECs, iPericytes, and iAstrocytes under normoxia and ischemia. f. Immunofluorescence images of VCAM-1 and ICAM-1 in iBMECs under normoxia and ischemia. Scale bars: 20 μm. g. Quantification of VCAM-1 and ICAM-1 fluorescence intensities under ischemia relative to normoxia. h. TEM images of iBMECs and iAstrocytes under normoxia and ischemia, revealing ultrastructural changes in cellular morphology. i. TEM images of tight junctions and adherens junctions in iBMECs under normoxia and ischemia. *: $P < 0.05$, **: $P < 0.01$, ***: $P < 0.001$. Representative images were obtained from three independent experiments. White arrows indicate tight junctions, and yellow arrows indicate adherens junctions. Scale bars: 5 μm (h, Normoxia-iBMECs, Normoxia-iAstrocytes, Ischemia-iBMECs and Ischemia-iAstrocytes, up), 5 μm (h, Ischemia-iBMECs, down), 2 μm (h, Normoxia-iBMECs, Normoxia-iAstrocytes, and Ischemia-iAstrocytes, down), 1 μm (i, left), 500 nm (i, right). Transmission electron microscopy, TEM. Transendothelial electrical resistance, TEER.

identified 517 commonly upregulated and 466 commonly downregulated genes across both endothelial and brain cells (Fig. 4b and c). These findings suggested a coordinated response to ischemic stress.

Gene ontology (GO) enrichment analysis further supported this notion, showing shared biological processes such as autophagy, cellular responses to stress, and apoptosis regulation in both iBMECs and brain cells (Fig. S1). Upregulated genes were associated with enhanced stress resistance, inflammation modulation, and autophagy activation, while downregulated genes reflected impaired mitochondrial function, protein synthesis, and cell proliferation—hallmarks of metabolic stress under ischemia. At the same time, the suppression of mitochondrial function points to compromised cellular bioenergetics, with both cell types attempting to manage mitochondrial damage.

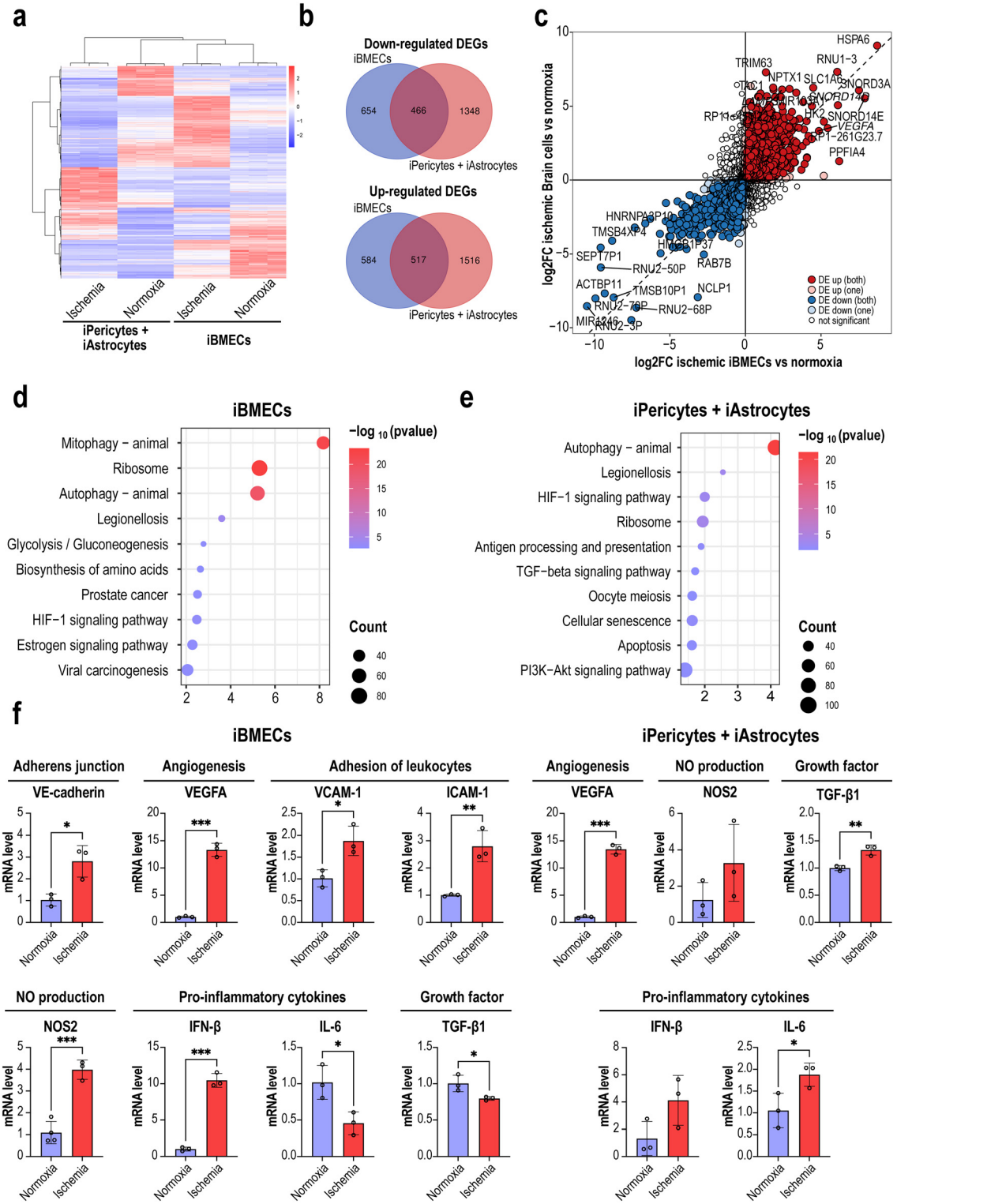

Fig. 4 Transcriptomic profiling reveals coordinated cellular responses to ischemic stress. a. Heatmap showing hierarchical clustering of differentially expressed genes (DEGs) in ischemia *versus* normoxia conditions for brain cells and iBMECs, with distinct transcriptional profiles observed between groups. b. Venn diagrams illustrating the overlap of upregulated and downregulated DEGs between brain cells and iBMECs under ischemic conditions. c. Fold change–fold change (FC–FC) plot showing the $\log_2$(fold change) of DEGs in ischemic BBB cells *vs.* normoxia (*y* axis) and ischemic iBMECs *vs.* normoxia (*x* axis). Genes that are DE in both or only one comparison are indicated. d and e. KEGG pathway enrichment analysis of DEGs in iBMECs (d) and brain cells (e). f. Quantitative analysis of mRNA levels for genes associated with adherens junctions (VE-cadherin), angiogenesis (VEGFA), leukocyte adhesion (VCAM1 and ICAM1), nitric oxide production (NOS2), pro-inflammatory cytokines (TNF-α, IFN-β, and IL-6), and growth factors (TGF-β1). Left: iBMECs; right: brain cells (iPericytes + iAstrocytes). Data are presented as the mean ± standard error of the mean (SEM) (n = 3). Statistical significance was determined using Student's t-test. Asterisks indicate importance: *: $P < 0.05$, **: $P < 0.01$, ***: $P < 0.001$. Differentially expressed genes, DEGs.

KEGG (Kyoto Encyclopedia of Genes and Genomes) pathway analysis revealed enrichment of hypoxia-adaptive and stress-related pathways (Fig. 4d and e). In brain cells, the HIF-1, TGF-β, and autophagy signaling pathways were prominent. iBMECs showed increased expression of inflammation-related and proteostasis-associated pathways. These pathways play critical roles in the cellular adaptation to hypoxia, promoting angiogenesis, cellular survival, and inflammatory responses.

We determined the key findings by examining the specific gene markers using qPCR analysis. In iBMECs, the expression of VE-cadherin, which is a core adherens junction protein, was significantly upregulated, potentially reflecting compensatory endothelial junctional remodeling under stress. The angiogenic factor VEGFA was markedly elevated, indicating a robust vascular response to hypoxia. Pro-inflammatory activation was evidenced by increased levels of VCAM-1, ICAM-1, IL-6, and IFN-β, consistent with endothelial immune reactivity. Notably, NOS2 expression also rose, suggesting enhanced nitric oxide production, a known hallmark of endothelial activation. TGF-β1, a multifunctional growth factor, was significantly regulated, potentially indicating involvement in tissue repair processes (Fig. 4f and S2). In brain cells, similar trends were observed. Upregulation of NOS2 and IL-6 reflected glial inflammatory responses, while increased TGF-β1 expression in brain cells (iPericytes + iAstrocytes) suggested a role in growth signaling and tissue remodeling. These findings collectively reveal that both endothelial and glial cells respond to ischemic challenge through coordinated upregulation of angiogenesis, inflammation, nitric oxide signaling, and growth factor-mediated repair pathways.

To further evaluate the clinical relevance of our *in vitro* model, we compared the transcriptomic profiles of our OGD-induced iBBB-on-a-chip with publicly available datasets of human ischemic stroke samples (GEO, GSE56267) and MCAO mouse models (GEO, GSE303321). Principal component analysis (PCA) demonstrated that iBBB-on-a-chip samples were more closely clustered with human samples, whereas mouse samples exhibited a distinct separation (Fig. S3), suggesting better transcriptomic fidelity to the human pathological state. GO enrichment analysis of the top PC1 loading genes revealed key hallmarks of ischemia-induced stress responses, including protein degradation, TORC1 regulation, and autophagy (Fig. S4). These results underscore the translational potential of our platform and its ability to capture disease-relevant molecular features.

3.4 Hub gene identification *via* co-expression modules and machine learning

To explore the molecular networks of the ischemic stroke-on-chip, we conducted a weighted gene co-expression network analysis (WGCNA) to identify co-expression modules strongly associated with ischemic characteristics. Modules were color-coded based on their hierarchical clustering, and their connection with ischemic or normoxic conditions was quantified. Among the identified modules, the yellow module demonstrated the strongest association with ischemic conditions, exhibiting highly significant correlations (Fig. 5a and b). This indicates that the yellow module plays a central role in the cellular response to ischemic stress, and its genes are strongly involved in the pathophysiology of ischemic events.

We further intersected genes from the ischemic-associated modules with DEGs identified in iBMECs, iPericytes, and iAstrocytes. This intersection analysis found 126 overlapping genes, which likely contribute to BBB dysfunction in stroke (Fig. 5c). As shown in Fig. S5, the ClueGO enrichment analysis identified key gene ontology (GO) terms associated with the intersected genes, such as lipopolysaccharide-mediated signaling, phosphofructokinase activity, and heat acclimation, reinforcing the cellular stress and metabolic adaptation responses to ischemic injury. Additionally, Fig. S6 shows the results of MCODE clustering for the intersected genes. This clustering revealed three distinct groups (clusters 1, 2, and 3) of highly interconnected genes, underscoring the collaborative nature of gene expression changes in response to ischemic stress. Cluster 1 (*e.g.*, UQCRC10 and MT-ND3) highlights mitochondrial dysfunction, cluster 2 (*e.g.*, HSPA1A/B and HSPA6) focuses on protein folding and stress response, and cluster 3 (*e.g.*, PFKP and PFKFB3) emphasizes metabolic adaptation. Pathway enrichment analysis confirmed that these genes play key roles in ischemic injury (Fig. 5d).

We then used random forest and LASSO regression to find the candidate genes for further functional validation. Random forest analysis ranked the top 30 genes based on their mean decrease accuracy and mean decrease Gini, providing insights into the genes with the greatest predictive importance for ischemic conditions (Fig. 5e, left). LASSO regression identified genes with the strongest coefficients, reflecting their statistical association with ischemia (Fig. 5e, center right). Integration of the two methods revealed five consensus hub genes: AARS, HSPA1B, UBL5, CCDC124, and EIF4E2 (Fig. 5e, bottom right).

3.5 Screening of small-molecule drugs for ischemic stroke

To explore potential therapeutic interventions targeting the identified hub genes, we performed small-molecule drug screening and validation using both *in silico* and experimental approaches. qPCR analysis confirmed the differential expression of the five hub genes in iBMECs, iPericytes, and iAstrocytes under ischemic conditions. All five genes showed significant regulation (Fig. S7).

Details of five hub proteins, AARS, HSPA1B, UBL5, CCDC124, and EIF4E2, are listed in Table S5. Structural modeling using AlphaFoldDB provided detailed 3D structures for these proteins, facilitating downstream docking studies (Fig. S8) Using the Connectivity Map (CMap) database, we identified ten candidate small molecules predicted to reverse

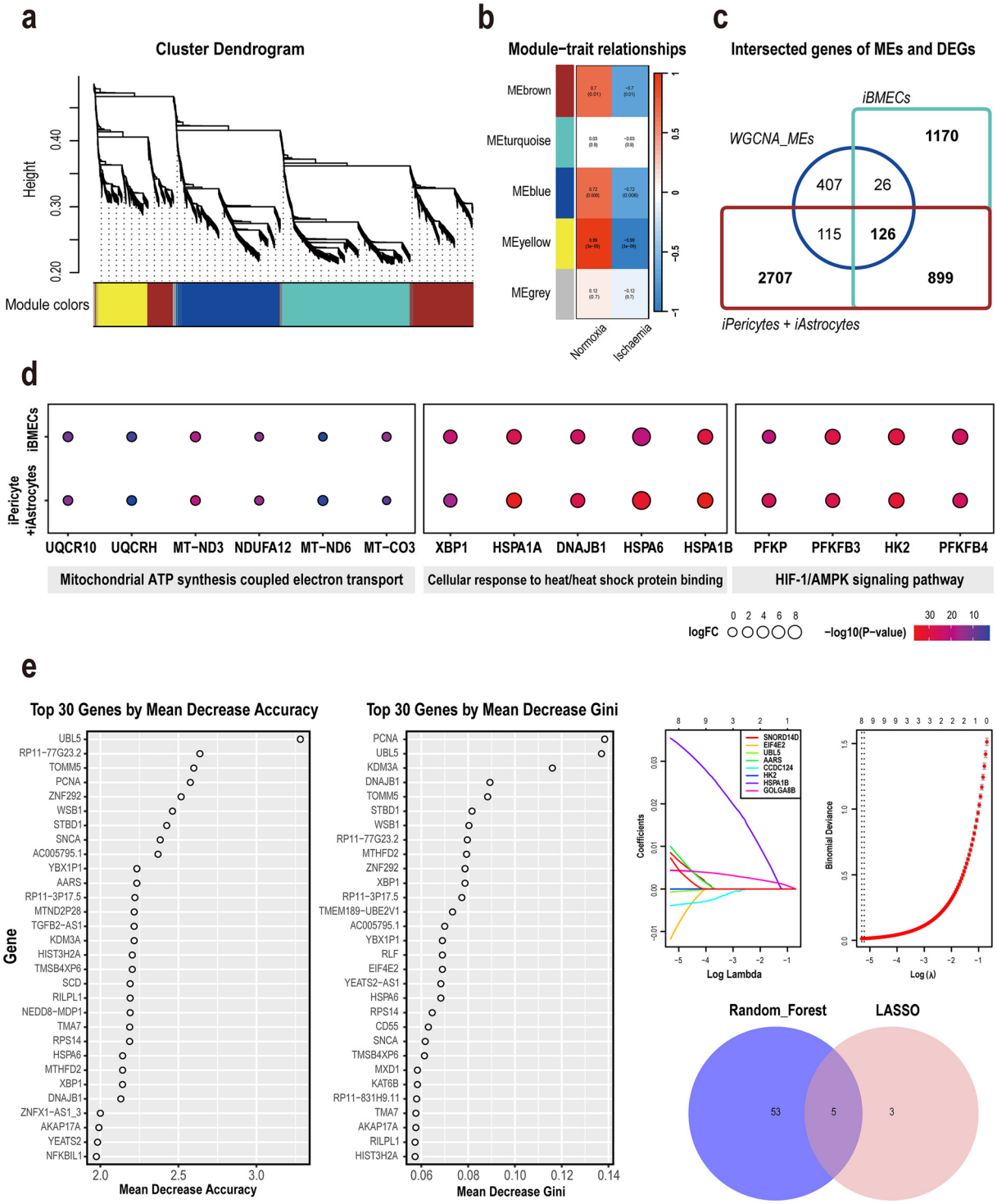

Fig. 5 Identification of hub genes *via* the co-expression network and machine learning. a. WGCNA cluster dendrogram showing hierarchical clustering of genes into distinct co-expression modules, represented by different module colors. b. Module–trait relationships depicting the correlation between identified co-expression modules and stroke-associated traits (normoxia *vs.* ischemia). Module significance (*P*-value) is indicated within each cell. c. Venn diagram of intersected genes from WGCNA modules (WGCNA_MEs) and differentially expressed genes (DEGs) in brain cells and iBMECs, identifying overlapping and unique gene sets. d. Key genes from significant modules enriched in three major pathways: mitochondrial ATP synthesis coupled electron transport, cellular response to heat/heat shock protein binding, and HIF-1/AMPK signaling. The dot size and color represent $\log_2$(fold change) (logFC) and $-\log_{10}$(*P*-value), respectively. e. Feature selection using random forest and LASSO regression. The top 30 genes ranked by mean decrease accuracy and mean decrease Gini (left) were identified, and the gene importance coefficients in LASSO analysis (center right) highlight significant predictors. The Venn diagram (bottom right) shows overlapping important genes between the two methods, identifying five consensus key genes. WGCNA, weighted gene co-expression network analysis.

ischemic-associated transcriptional signatures (Table S6). The therapeutic potential of the predicted compounds was confirmed through molecular docking studies using the Sybyl software, which assessed their binding affinities to the five hub proteins. Sybyl computes the interaction strength by integrating key factors such as steric fit, hydrogen bonding, hydrophobic effects, and electrostatics. Except for everolimus, for which no docking results were obtained, docking scores of other components provided quantitative evidence for their binding to ischemic-related proteins (Fig. 6a). Among the top candidates, coumarin emerged as a promising compound, demonstrating significant binding interactions with multiple target proteins across key ischemic-related pathways (Fig. 6b). A two-fact verification process was conducted using AutoDock underscoring coumarin's therapeutic potential as a versatile compound (Fig. S9). Both Sybyl and AutoDock analyses revealed that the ten small-molecule drugs have perfect binding affinities, especially coumarin, which forms stable interaction with residues critical for the function of ischemic-related proteins.

3.6 Functional validation of candidate drugs in the iBBB-on-a-chip model

To further validate the robustness and temporal applicability of our drug screening strategy, we established ischemic models with OGD durations of 3 h, 9 h, and 24 h, respectively, to capture the dynamic progression of ischemic injury. Two candidate compounds, coumarin (identified through computational screening) and everolimus (no results in molecular docking), were tested for protective efficacy. TEER measurements revealed that OGD exposure caused a time-dependent decline in barrier integrity, with the most pronounced disruption observed at 24 h. Both coumarin and everolimus treatment significantly preserved TEER values at all three time points, with maximal protection noted at 3 h and 9 h, indicating potential for early-phase intervention (Fig. 6c). In parallel, LDH assays demonstrated reduced cytotoxicity in brain cells upon coumarin or everolimus treatment, particularly at earlier time points (Fig. 6d), further supporting their neurovascular protective effects.

Building on these functional results, we next explored the molecular basis of coumarin's action by analyzing HSPA1B expression across BBB compartments. Considering the reported instability of GAPDH expression under hypoxic conditions (though variation <1.0 C_t in our platform), we included RPLP1 as a more stable reference gene to ensure data robustness. The results consistently showed that HSPA1B was upregulated in iBMECs ($P < 0.001$) but downregulated in brain cells ($P < 0.01$) upon coumarin treatment (Fig. S10), suggesting compartment-specific regulatory effects. This finding is in line with our MCODE module clustering and ClueGO pathway enrichment, such as heat acclimation pathways, confirming HSPA1B's potential role in mediating differential responses across the BBB interface and coumarin's protective effects.

We then extended experimental validation under the 24 h OGD + reperfusion setting. Butylphthalide was selected as the positive control drug.[37] At the same time, we also adopted two failed drugs, NXY-059 and minocycline, in a clinical test but succeeded in an animal model to confirm the advantage of our *in vitro* platform. Immunofluorescence results indicated that coumarin modestly enhanced ZO-1 expression, suggesting its potential to protect the blood–brain barrier. Butylphthalide and minocycline also partially restored ZO-1 levels, with notable effects in reducing inflammation, although their efficacy was inferior to that of coumarin (Fig. 6e). In contrast, NXY-059 exacerbated the damage, failing to effectively repair tight junctions, a phenomenon consistent with clinical trial results. This indicates that NXY-059 may not exert its expected neuroprotective effects under these specific conditions and may even worsen the injury. LDH changes also suggested coumarin's potential protective role by its dual effect—higher vascular LDH and lower brain LDH (Fig. 6f and g, S11). Together, these results support everolimus and coumarin as representative compounds with strong BBB-protective effects through both structural preservation and cytoprotection, mediated at least in part by modulation of ischemia-associated hub genes such as HSPA1B.

4 Discussion

In this study, we proposed a machine learning-driven strategy based on organ-on-a-chip technology to systematically investigate ischemic stroke-induced BBB dysfunction and facilitate small-molecule drug screening. We used iPSCs to construct an iBBB-on-a-chip model that recapitulated the functional features of the BBB during ischemic stroke conditions under OGD. Our results showed the characteristic features of ischemia-induced BBB impairment, such as disruption of endothelial tight junctions, pericyte fragmentation, and increased permeability. Further DEG analysis and enrichments revealed that different types of BBB cells engage in a unified response to ischemic injury, potentially contributing synergistically to the pathological process. Assisted by machine learning algorithms and drug databases, hub genes were identified to screen and validate coumarin as a candidate therapeutic compound with protective effects on the BBB. Everolimus also showed protective effects during time-point screening, further supporting the reliability of our screening strategy. These results emphasize the strength of our platform in linking computational predictions with functional validation for therapeutic discovery.

A key advantage of our model is its significantly higher TEER values, a crucial indicator of BBB integrity. While TEER can be influenced by technical factors (*e.g.*, membrane properties or measurement methods), the cell source is the major determinant.[38,39] Traditional *in vitro* BBB models, particularly those using primary endothelial cells, typically exhibit low TEER values in tens of $\Omega \times cm^2$, failing to

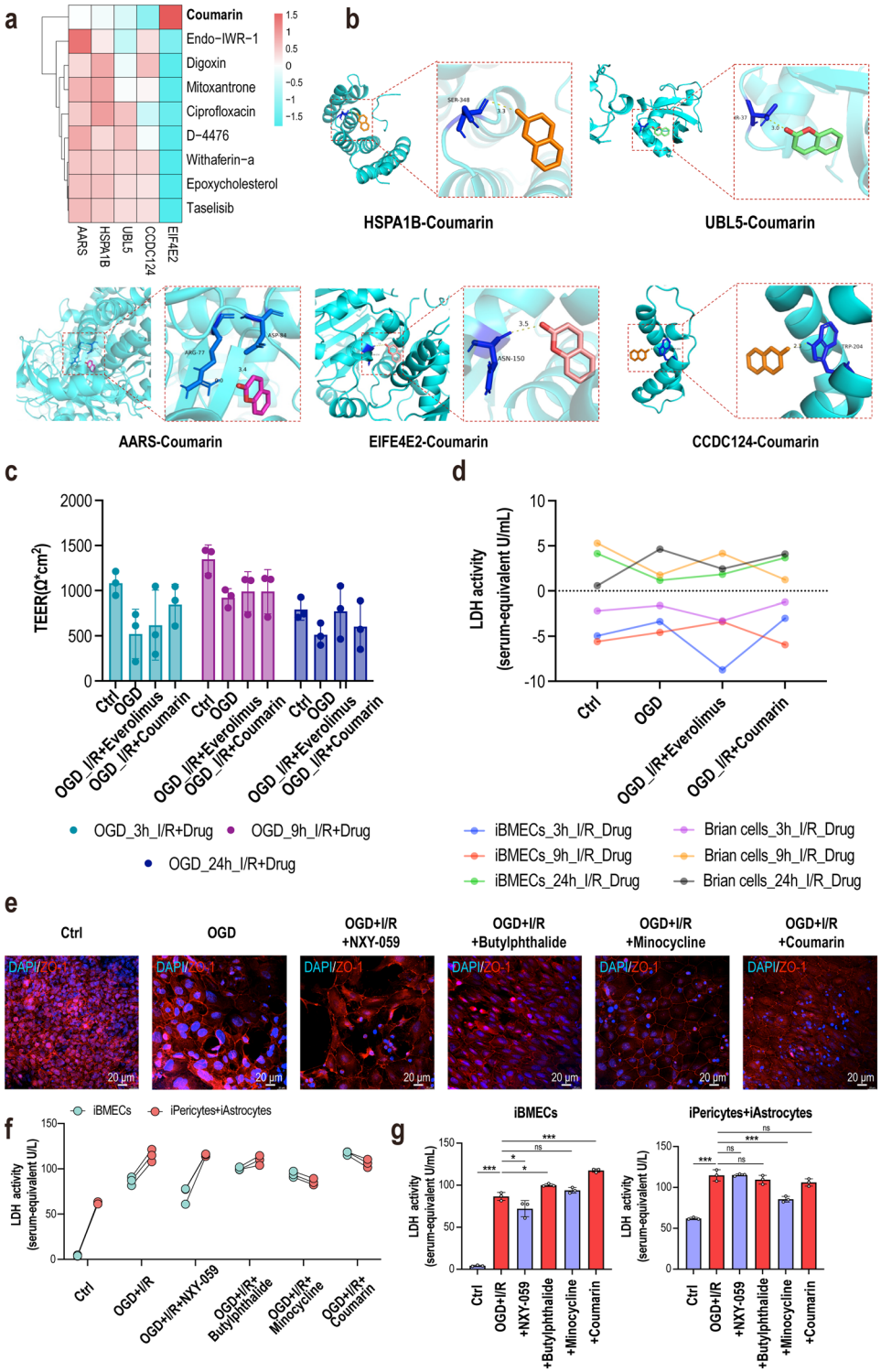

Fig. 6 Screening and validation of therapeutic compounds for ischemic stroke. a. Heatmap displaying the binding energy of the small-molecule drug and the hub protein. b. Small-molecule drug docking targets with the lowest binding energy. c. TEER measurements of the iBBB-on-chip under OGD + I/R conditions at 3 h, 9 h, and 24 h, with or without coumarin or everolimus treatment. TEER values were significantly reduced under OGD and restored upon drug intervention. d. Quantification of LDH activity in iBMECs and brain cells (iPericytes and iAstrocytes) at 3 h, 9 h, and 24 h post-OGD. LDH levels increased under ischemic conditions and were attenuated by drug treatment, indicating reduced cytotoxicity. Data are presented as the mean ± standard error of the mean (SEM) (n = 3). Negative values in relative LDH activity indicate that the measured absorbance in the treatment group was lower than the untreated control, suggesting minimal cytotoxicity or background correction artifact. e. Confocal micrographs of the iBBB-on-a-chip for ZO-1 (red) after 24 h-OGD exposure following 24 h-I/R + drug treatment (n = 3). f and g. LDH relative activity after 24 h-I/R + drug treatment. Data are presented as the mean ± standard error of the mean (SEM) (n = 3). Statistical significance was determined using one-way ANOVA with *post hoc* Tukey's test. *: $P < 0.05$, **: $P < 0.01$, ***: $P < 0.001$. I/R, ischemia/reperfusion. Transendothelial electrical resistance, TEER.

accurately reflect the robust barrier function of the human BBB *in vivo*.[40] In contrast, our iBBB-on-a-chip model achieves TEER values in the range of 1000–2000 $\Omega \times cm^2$, indicating enhanced tight junction formation and functional integrity. This improvement addresses the limitations of static models and improves physiological relevance. In addition to the cell source, our system incorporates mild oscillatory shear stress ($\sim 10^{-3}$ to 10^{-2} Pa) *via* dynamic rocking, mimicking disturbed flow relevant to stroke pathophysiology. Prior studies have shown that such low-magnitude shear can modulate the endothelial structure and inflammation, supporting our model's suitability for ischemic injury.[41–44] Using iPSC-derived iBMECs, iPericytes, and iAstrocytes ensures reproducibility and robustness, and also enables patient-specific modeling for personalized therapy.[45]

Notably, we observed the coordinated response to ischemic stress between iBMECs and brain cells. They have shared DEGs and concordant activation of key pathways, including autophagy, stress responses and inflammation. This suggests that the BBB is not merely a structural unit, but an integrated and dynamic system that responds collectively to pathological stimuli.[46–48] A spatiotemporal transcriptomic study in a mouse model from acute ischemia showed that cell activation, inflammation, and tissue remodeling were coordinated responses to ischemia in the lesion periphery.[49] Although some previous studies pointed out the roles of the BBB unit such as in stroke, systematic investigation of such cross-cellular coordination within a single *in vitro* model remains limited. Our results also illustrated the unique capacity of the organ-on-a-chip platform to recover multicellular interactions.

Using a combination of transcriptomic data and molecular docking, we found coumarin as a promising small-molecule therapeutic targeting hypoxia and ischemia-related pathways. The high binding affinity of coumarin to HSPA1B, AARS, and other hub proteins underscores its potential to modulate key processes such as proteostasis, mitochondrial metabolism, and cytoskeletal dynamics. A recent study showed that esculetin, a coumarin-derived phytochemical prevalent in traditional Chinese medicine, exhibits anti-acute ischemic stroke activities.[50] These findings further support the reliability of our platform in therapeutic screening. Coumarin's ability to restore barrier integrity and reduce inflammation in the iBBB-on-a-chip system highlights its therapeutic potential. However, additional *in vivo* studies are required to confirm its efficacy and safety. Furthermore, the exploration of combinatorial therapies targeting multiple pathways may enhance its therapeutic efficacy.

To further explore its mechanism of action, we focused on HSPA1B, a heat shock protein strongly implicated in the ischemic stress response. According to previous studies, it has been shown to regulate endothelial cell apoptosis and tight junction integrity under inflammatory or ischemic conditions.[51–53] Interestingly, coumarin induced a compartment-specific modulation: HSPA1B was upregulated in iBMECs but downregulated in brain cells. This bidirectional regulation likely represents a dual action, which may enhance endothelial stress resilience while mitigating parenchymal stress activation. These findings are consistent with the trends observed in LDH assays and echo the ClueGO enrichment of heat acclimation and unfolded protein response pathways, reinforcing the role of HSPA1B as both a biomarker and a functional effector of coumarin's protective effects.

Despite the current platform's strengths, several limitations remain. The model lacks immune cells such as microglia, which are known to modulate BBB function and drive neuroinflammatory cascades in stroke. Additionally, our chip adopts a planar transwell-like architecture, which does not fully recapitulate the 3D vascular geometry or laminar shear flow present *in vivo*. Future iterations will integrate microfluidic perfusion, circulating immune components, and lumenized vessels to more closely mimic the neurovascular niche.

In summary, this study provides a proof-of-concept framework for integrating an organ-on-a-chip and machine learning to decode disease mechanisms and accelerate therapeutic discovery. By modeling ischemic BBB disruption and identifying coumarin as a protective compound, we demonstrate the utility of this approach to bridge mechanistic insights with translational applications. While further validation in more complex models and patient-derived modeling is needed, this work provides a foundation for advancing translational research on BBB-associated neurological disorders and highlights the potential of combining engineered systems with computational tools to support mechanism-driven therapeutic screening.

Author contributions

Jiayue Liu, Peng Wang and Jianhua Qin conceived the project. Jiayue Liu and Peng Wang performed the experiments and analyzed the results. Peihan Lian collected and categorized the results. All authors discussed the results and commented on the manuscript. Jiayue Liu and Jianhua Qin wrote the manuscript and revised it.

Conflicts of interest

The authors declare that they have no conflicts of interest.

Data availability

Raw sequencing data have been submitted to the NCBI Sequence Read Archive (SRA) under accession number GSE294722. Publicly available transcriptomic datasets for comparative analysis were retrieved from the NCBI Gene Expression Omnibus (GEO), including GSE56267 (human stroke samples) and GSE303321 (mouse MCAO model). All other data supporting the findings of this study are available within the article and its supplementary information (SI). Supplementary information: the paper and its SI contain the primary data that support the findings of this investigation. Please see the supplemental materials in the uploaded files. See DOI: https://doi.org/10.1039/d5lc00517e.

Acknowledgements

The authors would like to thank Prof. Jianwen Deng (Peking University First Hospital) for kindly providing the iPSCs (#CN-IPS). The authors would like to thank Prof. Andy Peng Xiang (Sun Yat-Sen University) for kindly providing the iPSC-pericyte cells. The authors would like to thank Prof. Wenyuan Wang (Shanghai Institute of Organic Chemistry, Chinese Academy of Sciences) for kindly providing the iPSC-astrocyte cells. The authors would like to thank the Biomedical Platform at Suzhou Institute for Advanced Research of USTC for its equipment and technical support in bioimaging experiments. This research was supported by the National Key R&D Program of China (No. 2022YFA1104700), the National Natural Science Foundation of China (No. 32571340) and the National Science and Technology Major Project of China (No. 2025ZD0548601).

References

1 V. L. Feigin, M. H. Forouzanfar, R. Krishnamurthi, G. A. Mensah, M. Connor, D. A. Bennett, A. E. Moran, R. L. Sacco, L. Anderson, T. Truelsen, M. O'Donnell, N. Venketasubramanian, S. Barker-Collo, C. M. Lawes, W. Wang, Y. Shinohara, E. Witt, M. Ezzati, M. Naghavi and C. Murray, I. Global Burden of Diseases, S. Risk Factors and G. B. D. S. E. G. the, *Lancet*, 2014, **383**, 245–254.
2 J. Minnerup, B. A. Sutherland, A. M. Buchan and C. Kleinschnitz, *Int. J. Mol. Sci.*, 2012, **13**, 11753–11772.
3 A. Oddo, B. Peng, Z. Tong, Y. Wei, W. Y. Tong, H. Thissen and N. H. Voelcker, *Trends Biotechnol.*, 2019, **37**, 1295–1314.
4 A. Bhalerao, F. Sivandzade, S. R. Archie, E. A. Chowdhury, B. Noorani and L. Cucullo, *Fluids Barriers CNS*, 2020, **17**, 22.
5 R. Cecchelli, V. Berezowski, S. Lundquist, M. Culot, M. Renftel, M. P. Dehouck and L. Fenart, *Nat. Rev. Drug Discovery*, 2007, **6**, 650–661.
6 P. Ballabh, A. Braun and M. Nedergaard, *Neurobiol. Dis.*, 2004, **16**, 1–13.
7 B. Obermeier, R. Daneman and R. M. Ransohoff, *Nat. Med.*, 2013, **19**, 1584–1596.
8 N. J. Abbott, L. Ronnback and E. Hansson, *Nat. Rev. Neurosci.*, 2006, **7**, 41–53.
9 I. Sa-Pereira, D. Brites and M. A. Brito, *Mol. Neurobiol.*, 2012, **45**, 327–347.
10 G. C. Terstappen, A. H. Meyer, R. D. Bell and W. Zhang, *Nat. Rev. Drug Discovery*, 2021, **20**, 362–383.
11 N. M. O'Brown, S. J. Pfau and C. Gu, *Genes Dev.*, 2018, **32**, 466–478.
12 R. Rust, *J. Inflammation*, 2023, **20**, 21.
13 M. Jorfi, C. D'Avanzo, D. Y. Kim and D. Irimia, *Adv. Healthcare Mater.*, 2018, **7**, 1700723.
14 J. J. Jamieson, R. M. Linville, Y. Y. Ding, S. Gerecht and P. C. Searson, *Fluids Barriers CNS*, 2019, **16**, 15.
15 Y. Shi, L. Zhang, H. Pu, L. Mao, X. Hu, X. Jiang, N. Xu, R. A. Stetler, F. Zhang, X. Liu, R. K. Leak, R. F. Keep, X. Ji and J. Chen, *Nat. Commun.*, 2016, **7**, 10523.
16 E. Van Breedam and P. Ponsaerts, *Int. J. Mol. Sci.*, 2022, **23**, 7140.
17 S. Kawakita, K. Mandal, L. Mou, M. M. Mecwan, Y. Zhu, S. Li, S. Sharma, A. L. Hernandez, H. T. Nguyen, S. Maity, N. R. de Barros, A. Nakayama, P. Bandaru, S. Ahadian, H. J. Kim, R. D. Herculano, E. Holler, V. Jucaud, M. R. Dokmeci and A. Khademhosseini, *Small*, 2022, **18**, e2201401.
18 W. Bi, S. Cai, T. Lei and L. Wang, *Ageing Res. Rev.*, 2023, **87**, 101921.
19 B. Peng, S. Hao, Z. Tong, H. Bai, S. Pan, K. L. Lim, L. Li, N. H. Voelcker and W. Huang, *Lab Chip*, 2022, **22**, 3579–3602.
20 V. Guarino, A. Zizzari, M. Bianco, G. Gigli, L. Moroni and V. Arima, *Biofabrication*, 2023, **15**, 022003.
21 N. R. Wevers, A. L. Nair, T. M. Fowke, M. Pontier, D. G. Kasi, X. M. Spijkers, C. Hallard, G. Rabussier, R. van Vught, P. Vulto, H. E. de Vries and H. L. Lanz, *Fluids Barriers CNS*, 2021, **18**, 59.
22 Z. Lyu, J. Park, K. M. Kim, H. J. Jin, H. Wu, J. Rajadas, D. H. Kim, G. K. Steinberg and W. Lee, *Nat. Biomed. Eng.*, 2021, **5**, 847–863.
23 S. Kim, M. Kim, G. A. Grant and W. Lee, *Neural Regener. Res.*, 2024, **19**, 1431–1432.
24 W. Wei, F. Cardes, A. Hierlemann and M. M. Modena, *Adv. Sci.*, 2023, **10**, e2205752.
25 K. H. Yu, A. L. Beam and I. S. Kohane, *Nat. Biomed. Eng.*, 2018, **2**, 719–731.
26 R. J. Chen, J. J. Wang, D. F. K. Williamson, T. Y. Chen, J. Lipkova, M. Y. Lu, S. Sahai and F. Mahmood, *Nat. Biomed. Eng.*, 2023, **7**, 719–742.
27 A. Isozaki, J. Harmon, Y. Zhou, S. Li, Y. Nakagawa, M. Hayashi, H. Mikami, C. Lei and K. Goda, *Lab Chip*, 2020, **20**, 3074–3090.
28 T. E. Park, N. Mustafaoglu, A. Herland, R. Hasselkus, R. Mannix, E. A. FitzGerald, R. Prantil-Baun, A. Watters, O. Henry, M. Benz, H. Sanchez, H. J. McCrea, L. C. Goumnerova, H. W. Song, S. P. Palecek, E. Shusta and D. E. Ingber, *Nat. Commun.*, 2019, **10**, 2621.
29 Y. Wang, Y. Guo, P. Wang, J. Liu, X. Zhang, Q. Liu, L. Wei, C. Xu and J. Qin, *Commun. Biol.*, 2025, **8**, 669.
30 L. Yang, K. K. Shah and T. J. Abbruscato, *Methods Mol. Biol.*, 2012, **814**, 451–466.
31 J. J. Jamieson, Y. Lin, N. Malloy, D. Soto, P. C. Searson and S. Gerecht, *FASEB J.*, 2022, **36**, e22331.
32 P. Wang, Y. Wu, W. Chen, M. Zhang and J. Qin, *Biosensors*, 2022, **12**, 89.
33 P. Wang, L. Jin, M. Zhang, Y. Wu, Z. Duan, Y. Guo, C. Wang, Y. Guo, W. Chen, Z. Liao, Y. Wang, R. Lai, L. P. Lee and J. Qin, *Nat. Biomed. Eng.*, 2024, **8**, 1053–1068.
34 V. Singh, R. Kaur, P. Kumari, C. Pasricha and R. Singh, *Clin. Chim. Acta*, 2023, **548**, 117487.
35 E. Candelario-Jalil, R. M. Dijkhuizen and T. Magnus, *Stroke*, 2022, **53**, 1473–1486.
36 C. J. Frijns and L. J. Kappelle, *Stroke*, 2002, **33**, 2115–2122.
37 A. Wang, B. Jia, X. Zhang, X. Huo, J. Chen, L. Gui, Y. Cai, Z. Guo, Y. Han, Z. Peng, P. Jing, Y. Chen, Y. Liu, Y. Yang, F.

Wang, Z. Sun, T. Li, H. Sun, H. Yuan, H. Shao, L. Gao, P. Zhang, F. Wang, X. Cao, W. Shi, C. Li, J. Yang, H. Zhang, F. Wang, J. Deng, Y. Liu, W. Deng, C. Song, H. Chen, L. He, H. Zhao, X. Li, H. Yang, Z. Zhou, Y. Wang, Z. Miao and B. Investigators, *JAMA Neurol.*, 2023, **80**, 851–859.

38 M. Odijk, A. D. van der Meer, D. Levner, H. J. Kim, M. W. van der Helm, L. I. Segerink, J. P. Frimat, G. A. Hamilton, D. E. Ingber and A. van den Berg, *Lab Chip*, 2015, **15**, 745–752.

39 B. Srinivasan, A. R. Kolli, M. B. Esch, H. E. Abaci, M. L. Shuler and J. J. Hickman, *J. Lab. Autom.*, 2015, **20**, 107–126.

40 J. P. Vigh, A. Kincses, B. Ozgur, F. R. Walter, A. R. Santa-Maria, S. Valkai, M. Vastag, W. Neuhaus, B. Brodin, A. Der and M. A. Deli, *Micromachines*, 2021, **12**, 685.

41 R. M. Linville, M. B. Sklar, G. N. Grifno, R. F. Nerenberg, J. Zhou, R. Ye, J. G. DeStefano, Z. Guo, R. Jha, J. J. Jamieson, N. Zhao and P. C. Searson, *Fluids Barriers CNS*, 2022, **19**, 87.

42 R. M. Linville, J. G. DeStefano, M. B. Sklar, Z. Xu, A. M. Farrell, M. I. Bogorad, C. Chu, P. Walczak, L. Cheng, V. Mahairaki, K. A. Whartenby, P. A. Calabresi and P. C. Searson, *Biomaterials*, 2019, **190–191**, 24–37.

43 I. A. Tamargo, K. I. Baek, Y. Kim, C. Park and H. Jo, *Nat. Rev. Cardiol.*, 2023, **20**, 738–753.

44 L. Chen, H. Qu, B. Liu, B. C. Chen, Z. Yang, D. Z. Shi and Y. Zhang, *Front. Physiol.*, 2024, **15**, 1432719.

45 G. D. Vatine, R. Barrile, M. J. Workman, S. Sances, B. K. Barriga, M. Rahnama, S. Barthakur, M. Kasendra, C. Lucchesi, J. Kerns, N. Wen, W. R. Spivia, Z. Chen, J. Van Eyk and C. N. Svendsen, *Cell Stem Cell*, 2019, **24**(995–1005), e1006.

46 I. Wilhelm, A. Nyul-Toth, M. Suciu, A. Hermenean and I. A. Krizbai, *Tissue Barriers*, 2016, **4**, e1143544.

47 A. Herland, A. D. van der Meer, E. A. FitzGerald, T. E. Park, J. J. Sleeboom and D. E. Ingber, *PLoS One*, 2016, **11**, e0150360.

48 K. Arai, J. Lok, S. Guo, K. Hayakawa, C. Xing and E. H. Lo, *J. Child Neurol.*, 2011, **26**, 1193–1198.

49 D. Zucha, P. Abaffy, D. Kirdajova, D. Jirak, M. Kubista, M. Anderova and L. Valihrach, *Proc. Natl. Acad. Sci. U. S. A.*, 2024, **121**, e2404203121.

50 J. Q. He, R. L. Yuan, Y. T. Jiang, Y. Peng, J. R. Ye, S. S. Wang, L. Q. Li, Y. Ruan, P. Y. Li, X. Yan, W. B. He, G. Li, S. F. Chu, Z. Zhang and N. H. Chen, *Acta Pharmacol. Sin.*, 2025, **46**, 52–65.

51 J. Y. Kim, J. W. Kim and M. A. Yenari, *Neurosci. Lett.*, 2020, **715**, 134642.

52 P. Manikandan, R. Vijayakumar, B. Alshehri, S. Senthilkumar, M. S. Al-Aboody, A. Veluchamy and R. Haribaskar, *J. Infect Public Health*, 2022, **15**, 379–388.

53 J. Y. Kim, Y. Han, J. E. Lee and M. A. Yenari, *Expert Opin. Ther. Targets*, 2018, **22**, 191–199.